LITHOS 460-461 (2023) 107385

Contents lists available at ScienceDirect

LITHOS

journal homepage: www.elsevier.com/locate/lithos

Alteration of chromite during serpentinization of peridotites

Ruolin Liu [a], Junhong Zhao [a,b,*], Meifu Zhou [a,b], Han Qi [a]

[a] State Key Laboratory of Geological Processes and Mineral Resources, School of Earth Sciences, China University of Geosciences, Wuhan 430074, China
[b] State Key Laboratory of Ore Deposit Geochemistry, Institute of Geochemistry, Chinese Academy of Sciences, Guiyang, China

ARTICLE INFO

Keywords:
Chromite
Hydrothermal alteration
Trace elements
Jinchang ophiolite
South China

ABSTRACT

Trace element (Zn, Co, Mn, Ni, Ga, V, Ti, and Sc) compositions of chromite in mafic-ultramafic rocks are widely used for addressing their petrogenesis and discriminating tectonic environments, but they can be altered by subsolidus re-equilibration and hydrothermal alteration, and the detailed dynamic processes are not clear. The Jinchang ophiolite in SW China is part of the Tethyan ophiolite, and consists mainly of harzburgite with minor lherzolite. These peridotites are strongly serpentinized, and contain variably modified chromite and magnetite. Two types of chromite are identified in harzburgite, including magmatic and altered chromite. The magmatic chromite occurs as granular or amoeboid minerals, or as cores surrounded by the altered chromite, and they have homogeneous major elemental compositions ($Mg_{0.65}Fe_{0.35}(Cr_{0.46}Al_{0.54})_2O_4$), but their trace elements, such as Ni, Ga, V, Zn, Co, and Mn, are variably changed during subsolidus re-equilibration. The altered chromite consists of ferrous chromite ($Mg_{0.15}Fe_{0.85}(Cr_{0.46}Al_{0.11}Fe_{0.43})_2O_4$) and chromian magnetite ($Fe(Cr_{0.15}Fe_{0.85})_2O_4$), which were formed by two stages of hydrothermal alteration. They are depleted in Ga and Sc, and enriched in Zn, Co and Mn during the alteration, but their Ti, Ni and V are increased and decreased in the first and second stage, respectively. Thermodynamic modeling reveals that: (1) Reaction between magmatic chromite and olivine at the first stage of alteration produces ferrous chromite and chlorite under high temperature (610–470 °C) and increasing oxygen fugacity (ΔFMQ increasing from −1 to 3) and water-rich conditions; (2) Chromian magnetite is generated by further alteration of the ferrous chromite in the second stage alteration under low temperature (< 470 °C) and decreasing oxygen fugacity conditions (ΔFMQ decreasing from 3 to −4). In addition, the first stage alteration significantly changed trace-element compositions of the magmatic chromite compared with the second stage alteration that slightly modified the ferrous chromite. This study clarifies trace element migration of chromite in the silicate mineral-hydrothermal fluid system, indicating that chromite microstructures and trace elemental compositions can record the detailed serpentinization processes.

1. Introduction

Trace elements (Zn, Co, Mn, Ni, Ga, V, Ti, and Sc) in chromite are generally controlled by partial melting and fractional crystallization, and are sensitive to temperature and oxygen fugacity of basaltic magmas, and therefore are increasingly used to fingerprint compositions of parental melt and confine tectonic settings of their host rocks (Dare et al., 2009; González-Jiménez et al., 2015; Pagé and Barnes, 2009; Su et al., 2019; Uysal et al., 2016; Zhou et al., 2014). However, chromite can be chemically changed during subsolidus re-equilibration and metamorphism, making its compositions are indispensable in petrogenetic studies (Barnes, 2000; Bliss and Maclean, 1976; Burkhard, 1993; Evans and Frost, 1975; Mukherjee et al., 2010; Wylie et al., 1987). The detailed behaviors of trace elements in chromite under these two important geological processes are not well addressed.

Subsolidus re-equilibration between chromite and silicate minerals (i.e., olivine, pyroxene), occurring before hydrothermal alteration, can variably change their trace element compositions (Pagé and Barnes, 2009). The early studies reveal that such re-equilibration has an impact on rapidly diffusing divalent elements (Zn, Co, and Mn) which have similar characters with Fe^{2+}, although the behaviors of non-divalent trace elements (Ga, V, Ti and Sc) are not clear. In order to thoroughly constrain trace element characters of chromite during this pre-alteration process, comparison among magmatic chromites with different degrees of subsolidus exchange is necessary.

It has been widely accepted that magmatic chromite can be replaced

* Corresponding author at: State Key Laboratory of Geological Processes and Mineral Resources, School of Earth Sciences, China University of Geosciences, Wuhan 430074, China.
E-mail address: jhzhao@cug.edu.cn (J. Zhao).

https://doi.org/10.1016/j.lithos.2023.107385
Received 16 August 2023; Received in revised form 4 October 2023; Accepted 4 October 2023
Available online 10 October 2023

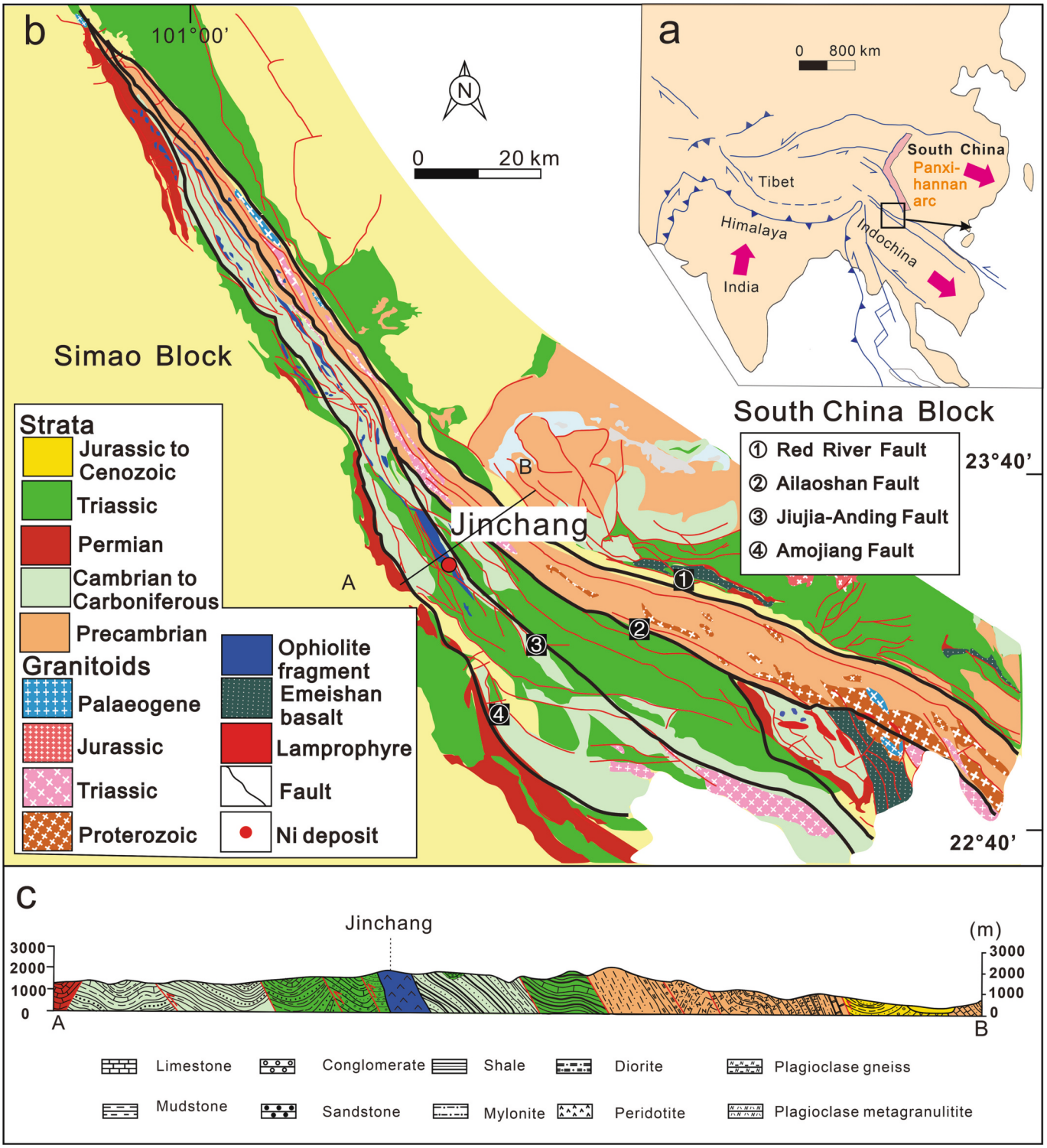

Fig. 1. (a) Tectonic framework of southeastern Asia with the location of the Ailaoshan tectonic zone. (b) Simplified regional geological map of the Jinchang ophiolites (after Yang et al., 2018). (c) Cross-section of the Jinchang ophiolites, its location is shown in (b).

by ferrous chromite (Fe^{2+}-rich chromite) and chromian magnetite (or Cr-bearing magnetite) during hydrothermal alteration (Gervilla et al., 2012; Kimball, 1990; Mellini et al., 2005). Recently, Eslami et al. (2021) proposed that ferrous chromite is formed by peridotite-water interactions under oxidizing conditions at the early stage of hydrothermal alteration, while chromian magnetite is produced under reducing conditions at the later stage of hydrothermal alteration. Chromite generally has stable major elemental compositions even after some degrees of hydrothermal alteration, but its trace elemental compositions and microstructures are sensitive to high and low temperature hydrothermal alterations, and thus are effective and crucial for addressing petrogenesis and tectonic settings.

Previous studies are mainly focused on trace elemental concentrations of chromite from ophiolitic peridotites or komatiitic rocks (Banerjee et al., 2022; Colás et al., 2014; Hu et al., 2022; Song et al., 2021), whereas little is known about their quantitative changes and dynamics

during the hydrothermal alteration. The Jinchang ophiolite is part of the Ailaoshan ophiolite belt that is a remnant of the Paleo-Tethys Oceanic lithopshere. The early studies are mainly focused on chronology and compositions of the mafic-ultramafic rocks (harzburgites, lherzolites, gabbro, diabase and basalt) (Hu et al., 2020; Yumul et al., 2008), while less work has been done for the conditions and geodynamic processes of the hydrothermal alteration during the serpentinization of peridotite. In this study, we provide new major and trace elemental data, in combination with thermodynamic modeling and micro-structure mapping to clarify alteration processes of the Jinchang ophiolite.

2. Geological background and petrography

South China consists of the Yangtze Block to the west and the Cathaysia Block to the east which were welted together during the Neoproterozoic (Zhao et al., 2011). The Jinshajiang-Ailaoshan suture zone represents the remnant of a major eastern branch of the Paleo-Tethys in China (Wang et al., 2000), its closure marks breakup of the Gondwana and formation of the eastern Asian Bock (Li et al., 2004; Metcalfe, 2002).

There are numerous mafic-ultramafic bodies exposed along the Jinshajiang-Ailaoshan structure zone (Fig. 1). They are part of the ophiolitic belt, which were formed during the Devonian and Carboniferous time (383–339 Ma) (Jian et al., 2009; Lai et al., 2014; Metcalfe, 2013; Stampfli and Borel, 2002), and tectonically emplaced due to collision between the Yangtze plate and the Simao-Indosinian plate during the late Triassic to Cenozoic (Fig. 1b) (Metcalfe, 1996; Mo and Pan, 2006; Zhang et al., 1995). The Mojiang ultramafic rock belt, ca. 87 km-long, is located between the Jiujia-Anding fault and the Amojiang fault (Fig. 1b). It comprises the Bailadu, Jinchang, Anding, Longtan, Mengli, and Midi mafic-ultramafic bodies from north to south.

The Jinchang mafic-ultramafic body is in fault contact with the upper Paleozoic Chahe Formation (slate, metamorphic sandstone and phyllite) to the east, and the upper Triassic Yiwanshui and Jinchangyan Formation (sandstone and shale) to the west and south. It consists of peridotites, gabbros, diabase and plagiogranite, which has been experienced greenschist facies metamorphism (Mo and Pan, 2006; Su, 2022). The serpentinised peridotite is the main rock type, and its protolith is dominated by harzburgite with minor lherzolite (Fang, 2003). Sheeted dikes, layered cumulate mafic and ultramafic rocks have not been identified in the sequence.

3. Analytical methods

3.1. Bulk rock compositions

Whole rock major elements were measured by X-ray fluorescence (XRF). 0.5 g rock powder and 5 g compound flux ($Li_2B_4O_7$:$LiBO_2$ = 12:22) were fused at ~1050 °C in 95% Pt–5% Au crucibles, and then the melt was swirled repeatedly and poured into a mould to form a thin flat-surfaced disc (34 mm diameter). The loss-on-ignition (LOI) was measured on dried rock powder by heating in a pre-heated corundum crucible to 1000 °C for 90 min and recording the percentage weight loss. XRF analysis was carried out on a Shimadzu XRF-1800 sequential X-ray fluorescence spectrometer, using a Rh-anode X-ray tube with a voltage of 40 kV and current of 70 mA. Calibration curves used for quantification were produced by bivariate regression of data from ~63 reference materials encompassing a wide range of silicate compositions. Precision (RSD) is better than 4% and accuracy (RE) is better than 3%. The measurement procedure and data quality were monitored by repeated samples (one in eight samples), USGS standard AGV-2 and Chinese National standards GSR- 1 and GRS-7.

3.2. Mineral compositions

Chromite and magnetite compositions were determined by a Link

Table 1
Major oxide compositions (in wt%), Cr# and Mg# of two types of chromtie (magmatic and altered chromite) and veined magnetite of representative samples in harzburgite from the Jinchang ultramafic rocks.

Mineral	Magma-tic	Magma-	Magma-	Magma-	Magma-	Magma-	Altered	Altered	Altered	Mt	Mt	Mt
	Chr	Chr	Chr	Chr	Chr	Chr						
Type	Granular	Granular	Granular	Amoeboid	Amoeboid	Core	Ferrous	Chromian	Chromian	Veined	Veined	Veined
							Chr	Mt	Mt	Mt	Mt	Mt
Sample	2–3	1–11	1–16	M2–2	M2–2	1–18	2–3	1–18	2–3	2–3	2–3	2–3
SiO_2	0.01	0.02	0.03	0.67	0.62	0.82	0.23	0.03	2.46	4.77	0.03	0.13	1.95	2.44	2.82
TiO_2	0.06	0.19	0.08	0.06	0.06	0.05	0.14	0.05	0.27	0.06	0.02	0.09	0.00	0.00	0.00
Al_2O_3	32.62	30.79	30.31	26.41	26.95	27.74	32.73	46.14	5.44	7.09	0.02	1.85	0.02	0.01	0.02
V_2O_3	0.00	0.00	0.00	0.21	0.22	0.22	0.00	0.00	0.00	0.00	0.00	0.00	0.01	0.00	0.00
Cr_2O_3	34.45	35.66	39.21	38.60	38.72	37.48	35.36	20.91	32.49	25.50	1.23	18.31	0.02	0.02	0.03
Fe_2O_3	1.14	3.56	1.13	1.98	1.46	1.41	2.20	3.33	23.85	25.12	66.05	46.72	62.78	62.61	61.86
FeO	16.40	13.09	14.43	18.49	18.42	18.41	11.99	11.07	17.70	25.74	32.31	26.34	37.31	36.68	36.83
MnO	0.31	0.26	0.28	0.51	0.36	0.38	0.60	0.23	8.70	3.58	0.21	3.59	0.01	0.02	0.02
MgO	13.63	15.79	15.09	11.97	12.17	12.36	16.68	18.84	5.57	6.71	0.26	1.84	1.27	1.75	1.87
CaO	0.00	0.02	0.00	0.01	0.01	0.02	0.00	0.00	0.04	0.00	0.00	0.00	0.07	0.11	0.11
Na_2O	0.02	0.00	0.00	0.00	0.00	0.00	0.00	0.00	0.04	0.02	0.03	0.03	0.00	0.00	0.00
ZnO	0.00	0.10	0.00	0.58	0.46	0.57	0.16	0.11	0.72	0.68	0.00	0.60	0.00	0.00	0.00
NiO	0.07	0.12	0.08	0.08	0.08	0.08	0.14	0.29	0.68	0.29	0.01	0.10	0.21	0.04	0.06
Total	98.70	99.60	100.63	99.56	99.52	99.52	100.22	100.99	97.96	99.56	100.16	99.60	103.65	103.68	103.62
Mg#	0.60	0.68	0.65	0.54	0.54	0.55	0.71	0.75	0.36	0.32	0.01	0.11	–	–	–
Cr#	0.42	0.44	0.47	0.50	0.49	0.48	0.42	0.23	0.80	0.71	0.97	0.87	–	–	–

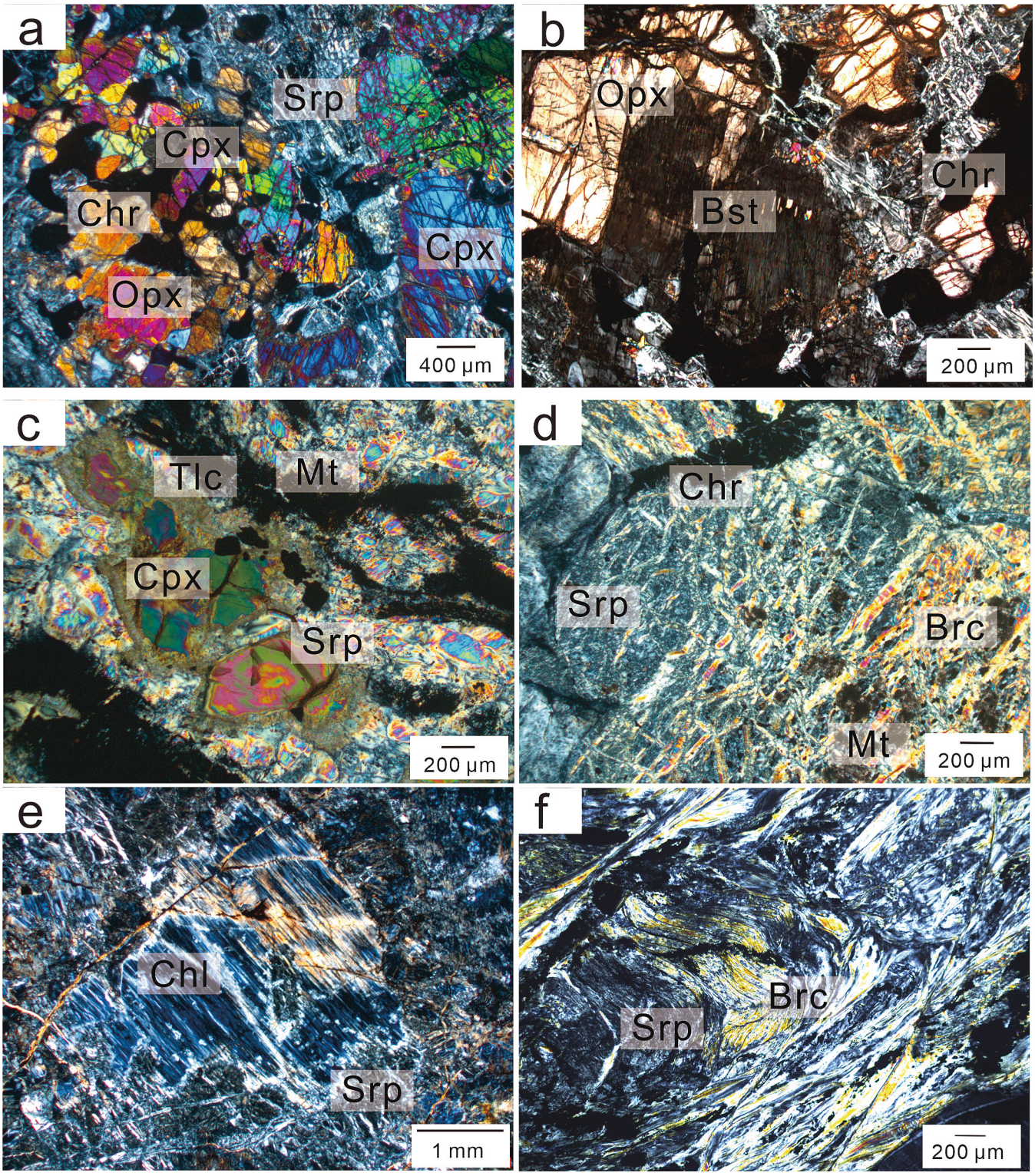

Fig. 2. Photomicrographs of the ultramafic rocks from the Jinchang ophiolite. (a) Fresh pyroxene and chromite in the serpentinized harzburgite. (b) Orthopyroxene locally serpentinized to bastite. (c) Clinopyroxene are partially replaced by talc rims. (d) Brucite veins formed networks in the serpentine. (e) Large chlorite grain with anomalous blue interference colors. (f) Deformed serpentine and brucite. Srp = serpentine, Chr = Chromite, Cpx = Clinopyroxene, OPX = Orthopyroxene, Bst = Bastite, Tlc = Talc, Mt. = Magnetite, Chl = Chlorite. (For interpretation of the references to colour in this figure legend, the reader is referred to the web version of this article.)

Energy Dispersive Spectrometry System connected to a JEOL JXA-8530 electron probe micro-analyzer (EPMA) at the State Key Laboratory of Ore Deposit Geochemistry (SKLODG), Institute of Geochemistry, Chinese Academy of Sciences (IGCAS). Analysis was carried out in a wavelength dispersive mode with a 15 kV accelerating voltage, 20 nA beam current and counting time of 10–20 s. A focused beam (1 μm) was used to avoid hitting any inclusions or exsolution lamellae within the grains. The Kα line was chosen for all analyzed elements. All data were

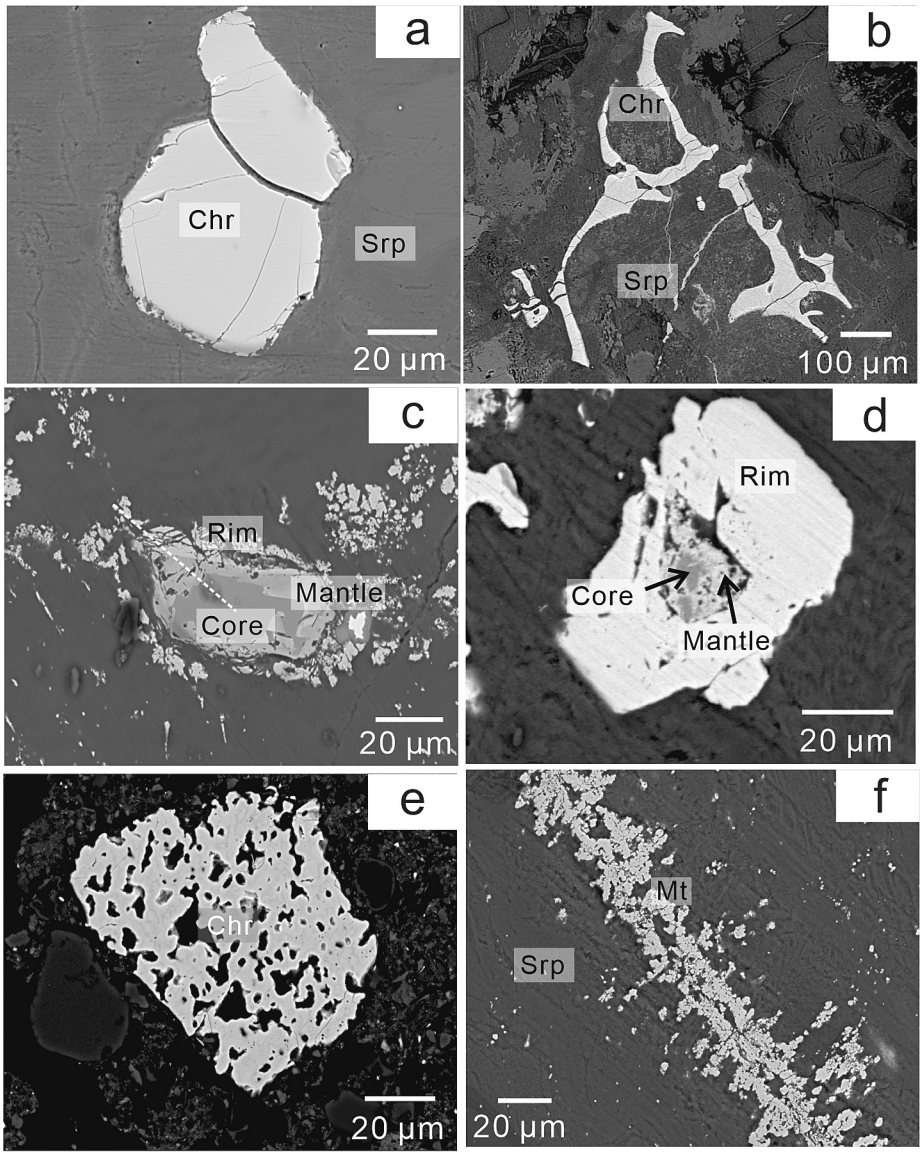

Fig. 3. BSE images of chromite and magnetite from the Jinchang ophiolite. (a) Subhedral to anhedral chromite grains enclosed in serpentine. (b) Amoeboid chromtie grains show elongated occurrence. (c) The altered chromite consists of magmatic chromite core, ferrous chromite mantle and chromian magnetite rim. (d) An altered chromite grain displays a thick chromian magnetite rim. (e) An altered chromite grain is completely transformed into porous texture and shows a sieve texture filled with chlorite. (f) Vein-shaped magnetite contains many tiny magnetite grains. Chr = chromite, Srp = serpentine, Chl = chlorite, Mt. = magnetite. The white line across chromite shows the locations of the zoning profile presented in Fig. 4.

corrected using the standard ZAF correction procedures. Besides quantitative spot analysis, wavelength dispersive spectrometers (WDS) maps were also collected. Fe^{2+} and Fe^{3+} were calculated by stoichiometry and charge balance. In order to acquire precise ferric iron data of chromite, $Fe^{3+}/\Sigma Fe$ ratios, estimated by stoichiometry, were further corrected using secondary spinel standards with $Fe^{3+}/\Sigma Fe$ ratios determined directly by Mössbauer spectroscopy (after Wood and Virgo, 1989).

In situ analysis was performed at the SKLODG of IGCAS using an Agilent 7900 ICP MS (laser ablation ICP MS) and a Coherent GeoLasPro 193 nm Laser Ablation system. A beam size of 38 μm was adopted for the ablation. The effect of sensitivity and mass discrimination from time dependent drift was corrected by analyzing the GSE-1G before and after every 10 examinations of the samples. Calibration was completed without internal standardization using multiple reference materials (GOR128-G, BCR 2G, BIR 1G, BHVO 2G, and GSE 1G). In this work, two reference materials (Cr and BC-28) were analyzed as unknown samples to monitor data quality. The ICPMSDataCal program was used to perform off-line selection and integration of background and analytical signals, time drift correction, and quantitative calibration after Liu et al. (2008). Analytical results of the international glass standards Cr and BC-28 are consistently within 10% of their reference values, with precision higher than 10% (relative standard deviation). The results of representative samples are listed in Table 1 (Total data seen in Table S1).

3.3. Thermodynamic modeling

Temperature-fO2 stability diagrams were calculated with Perple_X (version 6.9.0; Connolly, 2005) to investigate the influence of temperature and oxygen fugacity on chromite stability at 50 MPa. According to seismic velocity profiles, serpentinization occurs mostly within the first three kilometers of the oceanic lithosphere (Canales et al., 2000). The fluctuations in lithostatic pressure in these domains do not surpass 100 MPa, although temperature might vary by >400 °C. As a result, the differences of thermodynamic properties caused by pressure variations are minor compared to temperature variations. Thus, all numerical simulations were carried out at a constant pressure of 50 MPa. The

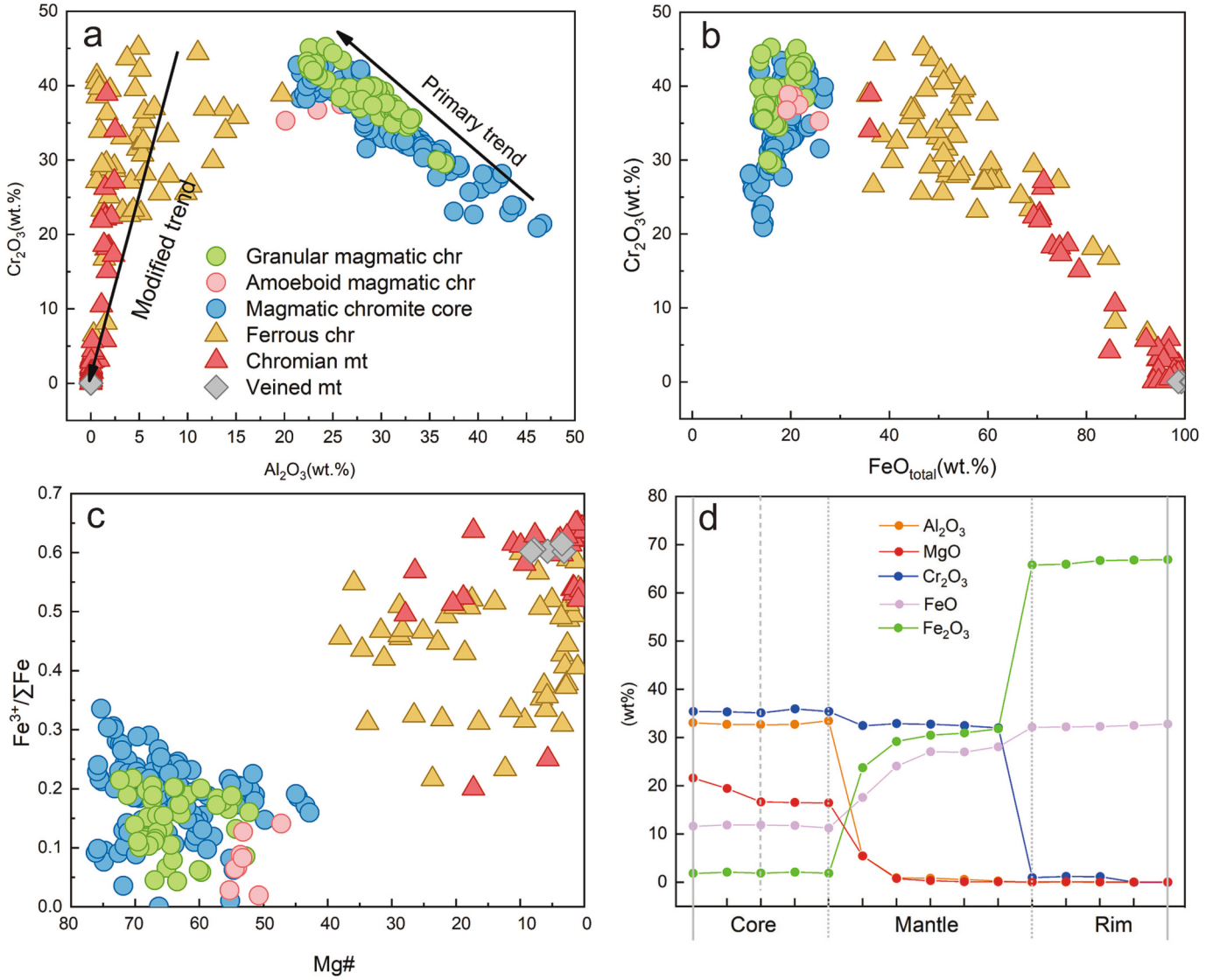

Fig. 4. Major elements variations for the chromite and magnetite from the Jinchang ophiolite. Chemical profile though a representative chromite grain (Fig. 3c) is also show for comparison (d).

calculation was performed using the mean composition of the Jinchang serpentinites (Si 35.76 mol%, Al 2.03 mol%, Cr 0.28 mol%, Fe 5.94 mol %, Mg 55.87 mol%, Ca 0.12 mol%), and ratio of water to rock is ~1. Thermodynamic equilibrium is assumed within centimeter scale (Evans et al., 2013). The thermodynamic database (Holland and Powell, 2011) was extended by including the dataset for chromium aqueous species, and the Fe-chromite and Mg-chromite endmembers (Huang et al., 2019; Klemme et al., 2009; Sverjensky et al., 2014). Mineral solid solutions include olivine (O(HP)), clinopyroxene (Cpx(HP)), chlorite (Chl(HP)) (Holland and Powell, 1996), antigorite (Atg(PN); Padrón-Navarta et al., 2013), brucite (B) and garnet (Grt(JH); Jennings and Holland, 2015). An additional chromite (CrSp) solid solution was added from Eslami et al. (2021) by using a reciprocal model based on the parameters for non-linearity in Gibbs energy from Sack and Ghiorso (1991).

4. Petrography of host serpentine, chromite and magnetite

The ultramafic rocks in this study are serpentinized harzburgites from the Jinchang ophiolite, and they are characterized primarily by protogranular textures crosscut by serpentine networks (Fig. 2a). The rocks are composed of serpentine (~70 vol%), orthopyroxene (~20 vol %), clinopyroxene (< 5 vol%), chromite (~2 vol%) and magnetite (~2 vol%) associated with minor accessory minerals (grossular and andradite ~1 vol%). The primary silicate minerals are mostly replaced by chlorite, and the only preserved fresh minerals are orthopyroxene and clinopyroxene crystals. Olivine is generally replaced by serpentines (Fig. 2a, c, and d), which are composed of lizardite, chrysotile and antigorite. Orthopyroxenes is subhedral to anhedral, 2 to 3 mm long, and are partially replaced by bastite (Fig. 2b). Kink banding and undulatory extinction are commonly observed in orthopyroxene grains. Clinopyroxene is much smaller in size (0.3–1.0 mm) relative to orthopyroxene (Fig. 2a). In addition, the serpentine generally developed fractures and sliding structures (Fig. 2f), indicating a sense of thrust of the Jinchang ophiolite. Talc, chlorite, tremolite, and brucite also occur as secondary altered minerals (Fig. 2c, d, e, and f). Talc commonly occurs as rims of serpentine grains (Fig. 2c), while brucite exists in serpentine networks (Fig. 2d and f), suggesting it was formed at the expense of olivine under stable conditions.

Chromite ranges in size from 0.01 to 0.5 mm, and is commonly distributed in serpentines, or occur as interstitial minerals among pyroxenes and chlorites (Figs. 2 and 3). Chromite grains have microfractures caused by volume expansion during serpentinization (Fig. 3a and b). It is divided into two types based on chemical compositions, including the magmatic and altered chromite. The magmatic chromite,

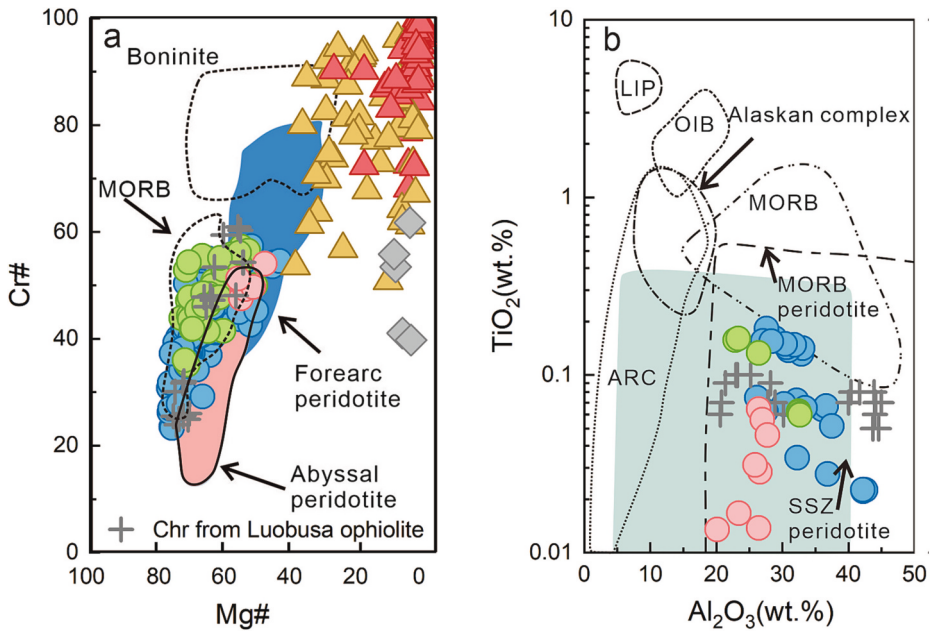

Fig. 5. Plots of Mg# vs. Cr# plot (a) and Al_2O_3 vs. TiO_2 plot (b) for the chromite and magnetite from the Jinchang ophiolite. Chromite from the Luobusa ophiolite (grey cross) is collected from Zhou et al., 2014. Other legends are the same as Fig. 4a.

generally occurs as granular (Fig. 3a) or amoeboid grains (Fig. 3b) or as core that are surrounded by the altered chromite rims (Fig. 3c and d), displays homogeneous characters both in thin sections and BSE images. The altered chromite consists of ferrous chromite mantle and chromian magnetite rims, and they display zoning images (Fig. 3c and d). The ferrous chromite generally preserves low to highly porous texture, now filled with Cr-chlorite, depending on size of chromite grain and degrees of serpentinization (Fig. 3e). The porous structure is eliminated by chromian magnetite as a result of intensive alteration (Fig. 3d).

In addition, veined magnetite is observed to be composed of fine euhedral magnetite grains ranging in size from 1 to 5 μm (Fig. 3f), joined together in serpentine, which may have resulted from the release of iron from olivine.

5. Chemical compositions of chromite and magnetite

The magmatic and altered chromite have different compositions (Fig. 4). EPMA line-analysis shows that each magmatic grain, including magmatic chromite core, exhibits constant chemical compositions although their edges have been altered (Fig. 4d). However, the magmatic chromite overall display variable Cr_2O_3 (20.92–45.21 wt%), Al_2O_3 (20.13–45.92 wt%), MgO (10.94–19.21 wt%) and FeO_{total} (11.49–25.75 wt%) (Table 1), and has an average composition of $Mg_{0.65}Fe_{0.35}(Cr_{0.46}Al_{0.54})_2O_4$. It has low Cr# (43 to 57) and high Mg# values (43 to 76), and fall in the field of forearc peridotite, and partially overlap the abyssal peridotite in the plot of Cr# vs. Mg# (Fig. 5a). It also has low TiO_2 (<0.732 wt%, avg. 0.23 wt%) and moderate Al_2O_3, and therefore all analysis is plotted within the field of SSZ-type peridotites (Fig. 5b). In the Cr-Al-Fe^{3+} plot (Fig. S1), the magmatic chromite displays low Fe^{3+} content and are similar to those of ophiolite and abyssal peridotite. They are enriched in Zn, Co, and Mn (especially Zn) and depleted in Sc and Ga, Ti, Ni, and display M-shaped positive Zn-Co-Mn anomalies (Fig. 6a). The amoeboid magmatic chromite has considerably low $Fe^{3+}/(Fe^{3+}+Fe^{2+})$ ratios (avg. 0.08), low Ga, Ti and Ni and higher Zn, Co and Mn, than the granular magmatic chromite (Figs. 4c and 6a).

Two generations of the altered chromite also differ in terms of chemical compositions. The ferrous chromite has high FeO_{total} (79.34–34.75 wt%), low MgO (7.74–0.17 wt%) and Al_2O_3 (19.75–0.58 wt%), and variable Cr_2O_3 (45.10–16.76 wt%), with on average composition of $Mg_{0.15}Fe_{0.85}(Cr_{0.46}Al_{0.11}Fe_{0.43})_2O_4$ (Fig. 4 and Table S1). They have variable Cr# (51–97), high Mg# values (43–76) and low $Fe^{3+}/(Fe^{3+}+Fe^{2+})$ ratios (avg. 0.45, 0.22–0.62). The chromian magnetite has low Cr_2O_3 (27.13–1.88 wt%), Al_2O_3 (< 2.43 wt%) and MgO (< 6.92 wt%), and high FeO_{total} (98.71–67.16 wt%, mainly Fe_2O_3), with an average composition of $Fe(Cr_{0.15}Fe_{0.85})_2O_4$(Cr# = 72–100, Mg# = 1–42, $Fe^{3+}/(Fe^{3+}+Fe^{2+})_{avg}$ = 0.60, 0.20–0.65).

The ferrous chromite and chromian magnetite have similar Ti, Ni, V and Sc, and higher contents of Zn (4306–8507 ppm), Co (226–817 ppm) and Mn (13933–26,827 ppm), but lower Ga (2–21 ppm) than the magmatic chromite (Zn:1054–14,919 ppm, Co:254–523 ppm, Mn:859–14,054 ppm, Ga:14–63 ppm; Fig. 6b).

The veined magnetite has Cr# numbers with an average of 0.50, but higher Fe_2O_3 (63 wt% avg) than the chromian magnetite (0.93, 56 wt%, respectively; Figs. 4 and 5a). They are depleted in Ti, Ni, V, Sc, Zn, Co and Mn relative to the chromian magnetite (Ti: 277–694 ppm, Ni: 1193–1915 ppm, V: 625–1126 ppm, Sc: 0.7–6.8 ppm, Zn: 4306–7635 ppm, Co: 226–817 ppm, Mn: 14555–21,628 ppm; Fig. 6d). The chlorite associated with ferrous chromite has composition of $Mg_{9.7}Al_{1.3}Cr_{0.1}Fe_{0.9}Al_2Si_6O_{20}(OH)_{16}$ (Table S1).

6. Discussion

6.1. Subsolidus re-equilibration in the magmatic chromite

Given high silicate/chromite ratios in Jinchang ophiolite, the magmatic chromite in this region may have experienced subsolidus re-equilibration before the hydrothermal alteration (Barnes and Roeder, 2001). Magmatic chromite generally partitions Mg and Fe with the surrounding silicate minerals, and result in formation of Mg-rich olivine and Fe-rich chromite through reaction of $Mg_{chromite} + Fe^{2+}_{olivine} = Mg_{olivine} + Fe^{2+}_{chromite}$ (Scowen et al., 1991). The magmatic chromite in this study generally has wide range of Mg# (43–76) and a narrow range of Cr# values (43 to 57), which means that Mg and Fe are rapidly diffused between olivine and chromite while Cr and Al slowly (Fig. 5a, Arai, 1994; Wan et al., 2008; Spandler and O'Neill, 2010). Their trace elements, such as Zn, Co, Mn, Ga and V are negatively, while Ni positively correlated with Mg# values (Fig. 7).

The granular and amoeboid magmatic chromite experiences

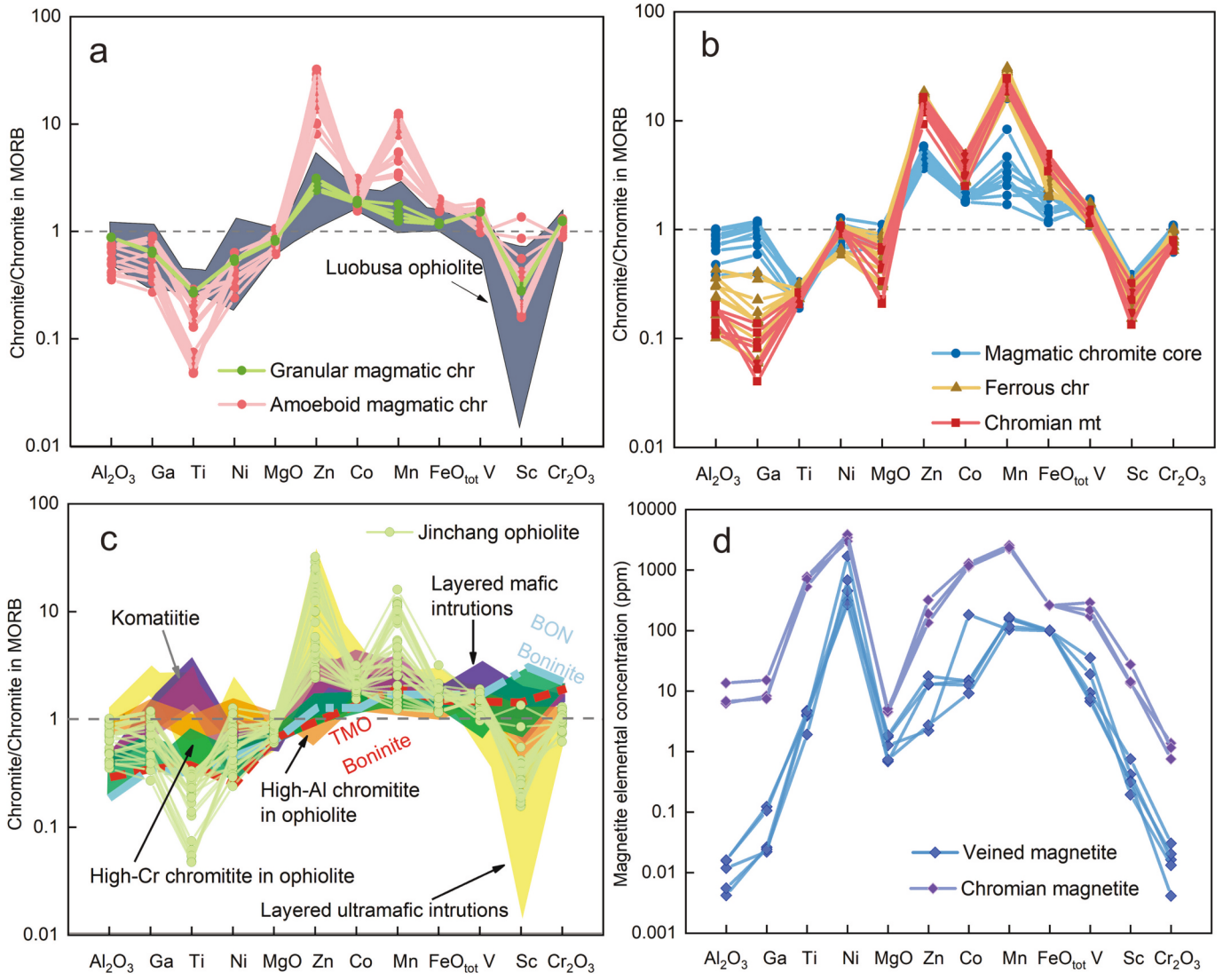

Fig. 6. Trace element spidergrams for the chromite and magnetite from the Jinchang ophiolite. Chromite from the Luobusa ophiolite (Zhou et al., 2014), the fore-arc ophiolite from the Thetford Mines and boninite lavas (Pagé and Barnes, 2009), the back-arc ophiolites from Cuba and Philippines, as well as those from komaiites, layered mafic (González-Jiménez et al., 2015) and ultramafic intrusions (Song et al., 2020) are shown for comparison. The normalizing chromite is from the East Pacific Rise MORB (Pagé and Barnes, 2009).

different degrees of Mg—Fe exchange during subsolidus re-equilibration. Isocon method was used in this study to constrain trace elemental variations (Grant, 1986; Guo et al., 2009). The high-Mg magmatic chromite (Mg# > 0.65) is considered as the primitive minerals which were not modified significantly by the subsequent subsolidus re-equilibration. Cr is considered as an immobile element, and mass changes of the other elements were calculated based on their deviations from isocon. The composition of each chromite can be scaled by multiplying the elemental concentration by standardization factor (Fig. 8a and b). Chromite composition with high Mg# is further subtracted from the scaled mineral composition to calculate the transfer ratios (Fig. 8c and d).

Calculations reveal that the divalent elements are more mobile than the non-divalent elements during subsolidus re-equilibration (Fig. 8c). Zn and Mn are the most mobile elements. The granular chromite has low mass gain for Zn (17.75%), Mn (27.21%), Co (5.60%), Ga (1.62%) and V (1.88%) than those of the amoeboid chromite (Zn = 364.29%, Mn = 237.29%, Co = 60.22%, Ga = 28.58% and V = 8.40%). The amoeboid magmatic chromite has high transfer ratios of Zn, Co, Mn, Ga, and V, indicating larger extents of re-equilibration, which may have resulted from their irregular shapes and large grain size (50 μm to 1 mm) that produce high circumference-to-area ratios relative to the granular chromite (Fig. 3b). Zn, Co and Mn form right decline M-shaped patterns (Figs. 6a and 8c) due to their decreasing partition coefficients in chromite (D_{Zn}^{Chr} =6.9–10.1, D_{Co}^{Chr} =3.83–6.03, D_{Mn}^{Chr}=0.876–1.11; Horn et al., 1994; Righter et al., 2006). The trend of trace element variation during subsolidus re-equilibration is quite different from that in the later hydrothermal alteration process.

6.2. *Two stages of chromite hydrothermal alteration*

Trace element concentrations in altered chromite are controlled by several factors, including element concentration in the hydrothermal liquid from which it crystallizes, partition coefficient, temperature, pressure, oxygen fugacity (fO_2), cooling rate, as well as competition with the other minerals crystallized at the same time (Dare et al., 2014). The altered chromite consists of ferrous chromite and chromian magnetite (Fig. 3c and d), which show different microstructures and elemental compositions (Table 1). They both have comparable V, Ti and Ni, but higher Zn, Co and Mn and lower Ga, Sc than those of the magmatic chromite core (Figs. 6b, S2 and S5). The isocon method is also used to

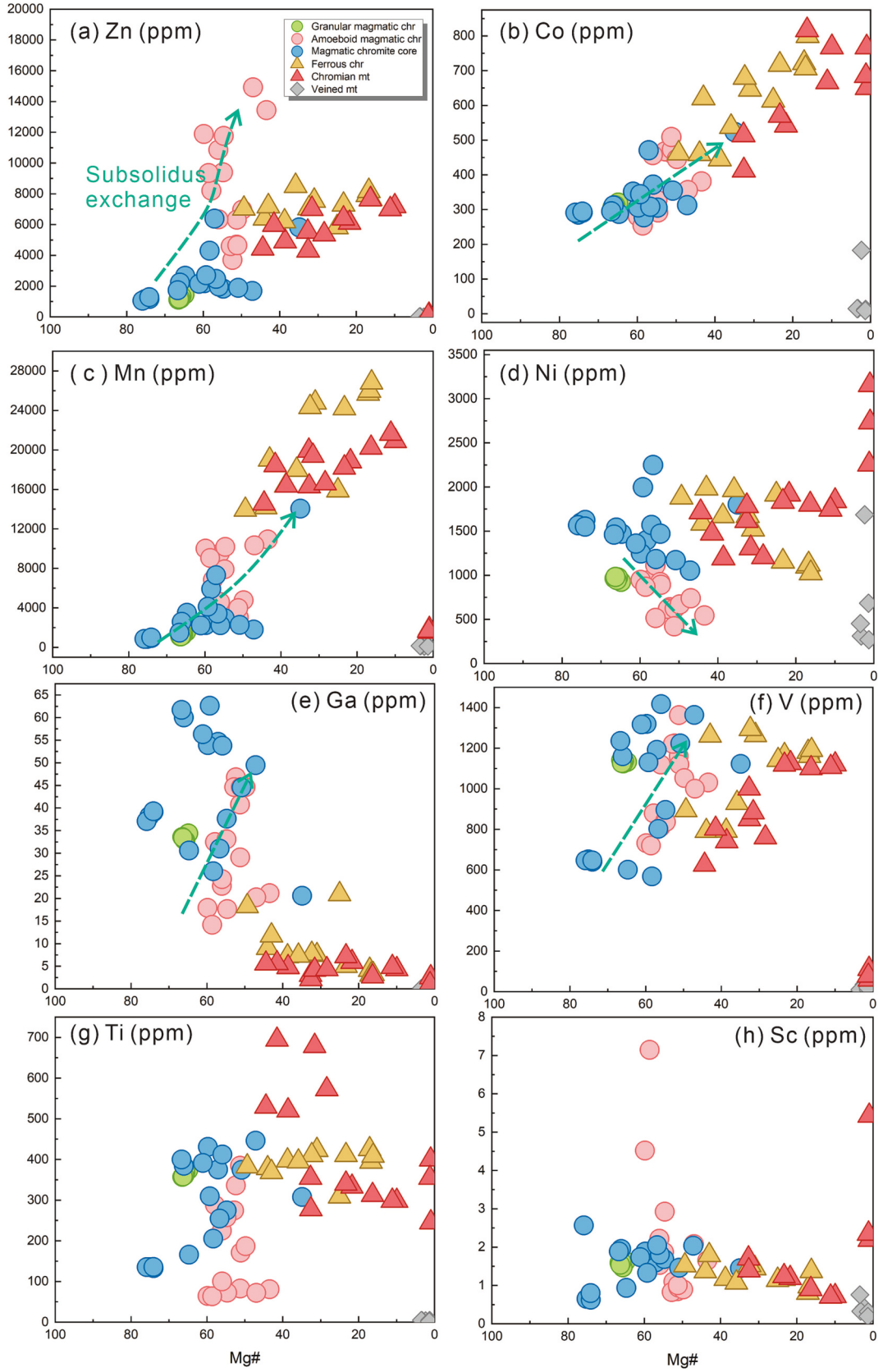

Fig. 7. Plots of trace elements against Mg# values for the magmatic chromite, altered ferrous chromite and chromian magnetite from the Jinchang ophiolite.

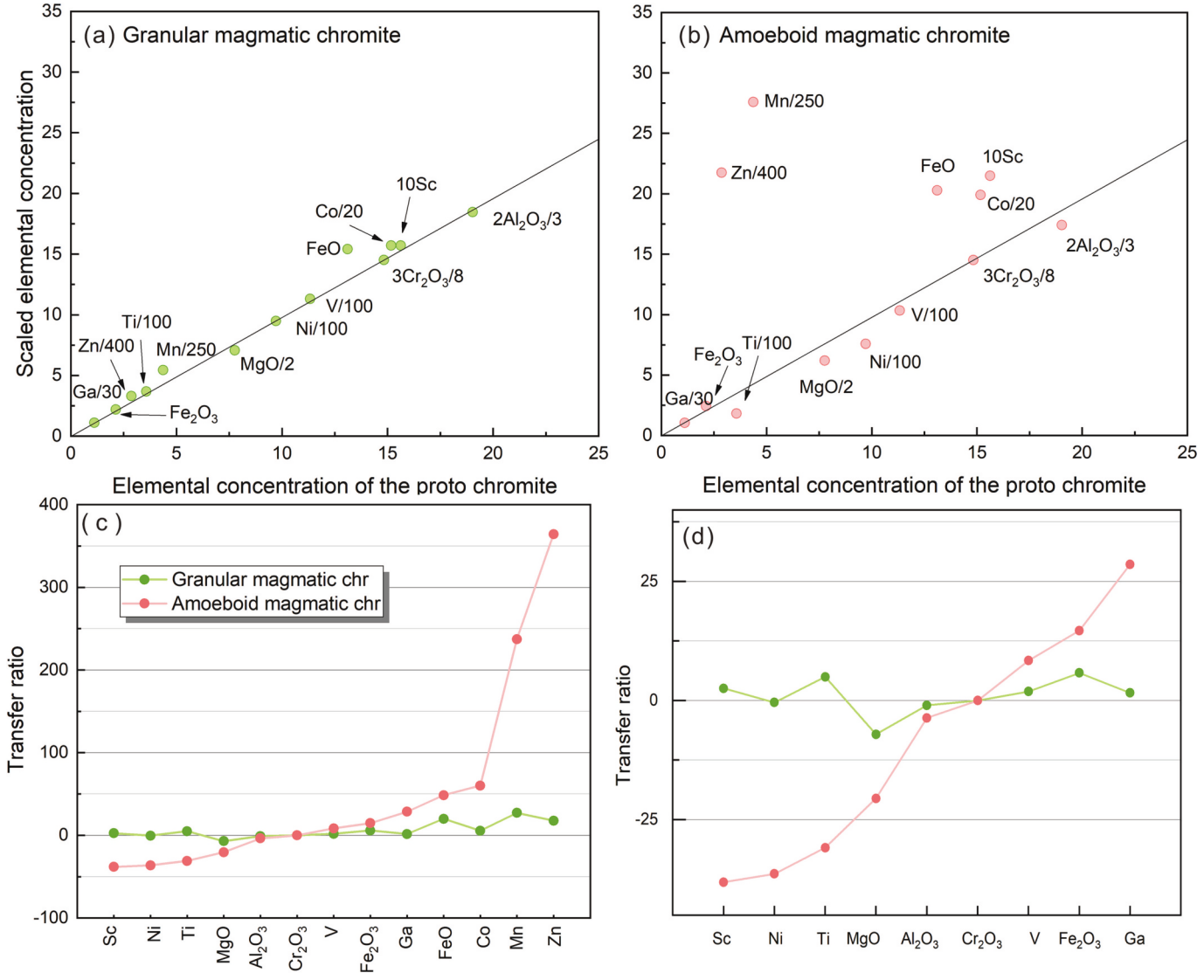

Fig. 8. Isocon diagrams and transfer ratio plot for the magmatic chromite from the Jinchang ophiolite.

evaluate elemental transfer in the ferrous chromite and chromian magnetite during the hydrothermal alteration (Fig. 9). The average composition of the magmatic chromite cores is supposed to be proto-composition. Cr solubility is 7 to 8 orders of magnitude lower than Fe (Eslami et al., 2021), and thus is considered as an immobile element during the hydrothermal alteration.

The ferrous chromite has higher Ti (11.8%) and Ni mass gain ratios (28.6%) than those of the chromian magnetite (8.0% and 9.5%), suggesting the two elements were released from the ferrous chromite in the second alteration stage (Fig. 9c). V occupies the octahedral site in chromite structure and occurs as V^{3+} with minor V^{4+} at low oxygen fugacity, which have similar compatibilities during the alteration (Balan et al., 2006; Toplis and Carroll, 1995), but becomes incompatible at high oxygen fugacity (Bordage et al., 2011). The ferrous chromite gained 3.5% V, which may have resulted from its more available octahedral sites than those in the magmatic chromites, whereas the chromian magnetite loss 2.3% V probably due to reorder of Fe^{2+} and Fe^{3+} that promote substitution of Fe^{3+} by V.

Mn (398%, 453%), Co (78% and 105%) and Zn (153% and 186%) continually increase from the magmatic core to the ferrous chromite and chromian magnetite (Fig. 9c), and they form left-decline Zn-Co-Mn patterns (Fig. 6b).

Compared with the magmatic chromite core, the ferrous chromite and chromian magnetite have low Ga and Sc (Fig. 9c and d). Ga abundance is controlled by distribution of trivalent cations in the altered chromite (Colás et al., 2014). Low Ga concentrations in the ferrous chromite may have resulted from consumption by the newly formed chlorite (Fig. 3c and d), whereas those in the chromian magnetite caused by Fe^{3+} replacement (Dare et al., 2009; Song et al., 2021). The relatively low Sc in the altered chromites probably due to a significant mass gain of other trace elements.

6.3. *Conditions of two stages of the hydrothermal alteration*

Thermodynamic modeling is used to constrain the conditions of the hydrothermal alteration. The pseudosection is calculated based on the average composition of the ultramafic rocks from the Jinchang serpentinite at 50 MPa. The results are plotted in the $\log_{10}fO_2$-T diagram (Fig. 10), in which the chromite solid solution is contoured by X_{Al} (molar ratios of Al/Al + Cr + Fe^{3+}), X_{Cr} (Cr/Al + Cr + Fe^{3+}) and $X_{Fe^{3+}}$ (Fe^{3+}/Al + Cr + Fe^{3+}). The path of alteration is constrained by the composition of the magmatic chromite core and altered chromite.

The modeling results show that chromite compositions are very sensitive to temperature and fO_2. The magmatic chromite from the Jinchang peridotite experienced two stages of alteration. During the first stage, in the field of Ol + Chr + Chl + Amp + Tc, the magmatic chromite

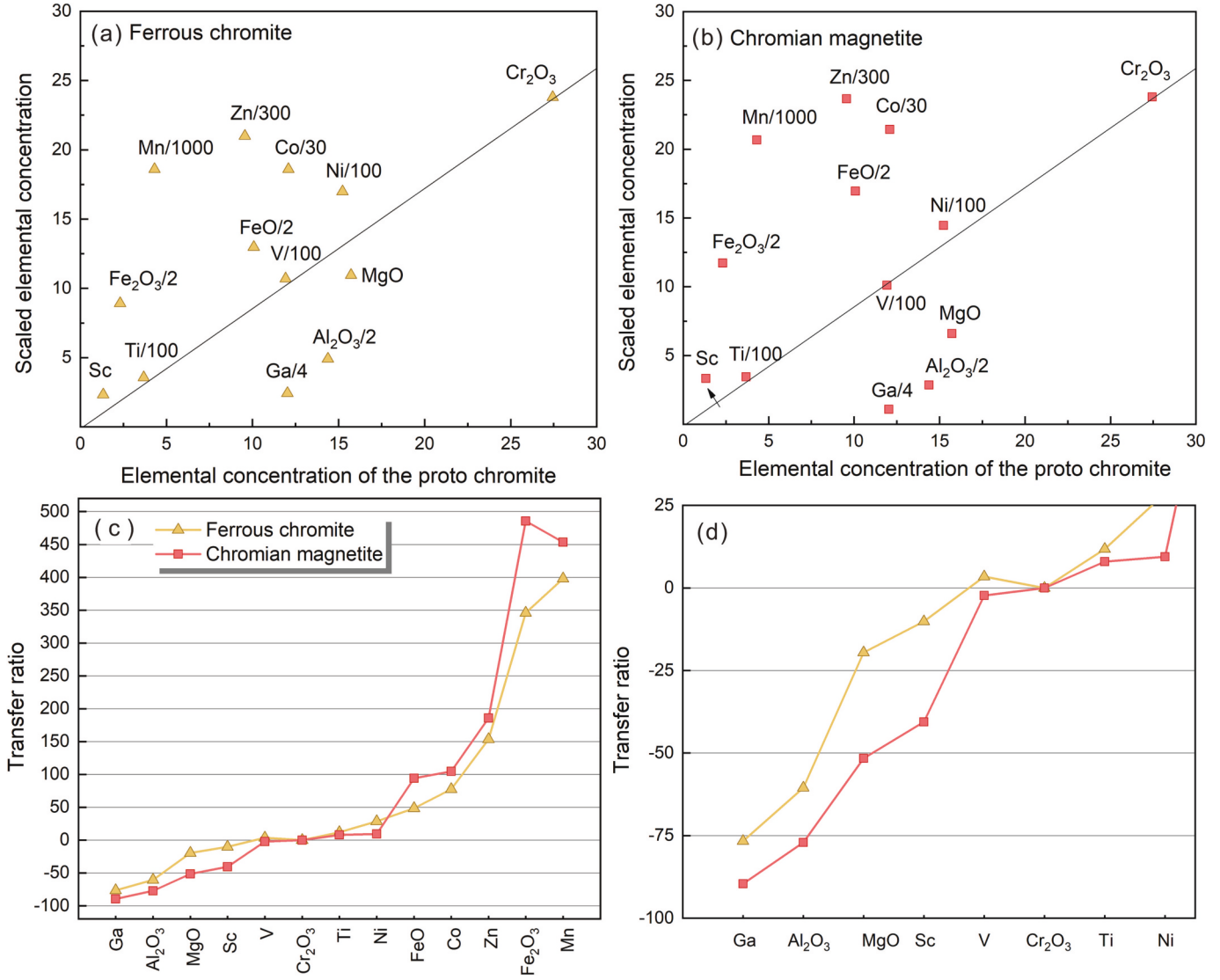

Fig. 9. Isocon diagrams and transfer ratios for the altered ferrous chromite and chromian magnetite from the Jinchang ophiolite. (a) Isocon diagrams for ferrous chromite. (b) Isocon diagrams for chromian magnetite. (c) Transfer ratios of major and trace elements in ferrous chromite and chromian magnetite. (d) A close-up of the transfer ratios in (c).

and olivine are replaced by the ferrous chromite and chlorite under high temperatures (610–470 °C) with an increase from −1 to 3 in ΔFMQ (Fig. 10). These parameters are compatible with those of the high-temperature hydrothermal alteration at mid-ocean ridges (Hasenclever et al., 2014). The alteration process can be accelerated by infiltration of the oxidative fluids through normal faulting, fissuring and cracking in the extensional environment (Mével, 2003). The ferrous chromites display porous microstructure, now filled with chlorite, which may have resulted from fluid dissolution (Fig. 3c and d), and their X_{Al} (0.66 to 0.33) and X_{Cr} (0.27 to 0.45) are rapidly changed with decreasing temperature.

$$3(Mg,Fe)(Cr,Al)_2O_4\ (\text{magmatic chromite}) + 6(Mg,Fe)_2SiO_4\ (\text{olivine}) + 8H_2O\ (\text{fluids}) + 6O_2\ (\text{oxygen}) = 5(Mg,Fe)(Cr,Al,Fe)_2O_4\ (\text{ferrous chromite}) + (Mg,Al,Cr,Fe)Al_2Si_6O_{20}(OH)_{16}\ (\text{chlorite}) \quad (1)$$

Reaction between olivine and fluids generates H_2 and veined magnetite at the second alteration stage (McCollom and Bach, 2009). Chromian magnetite is also generated around the ferrous chromite, and its X_{Cr} decreases from 0.45 to 0.01, and $X_{Fe^{3+}}$ increases from 0.90 to 0.95 (Fig. 10). Thermodynamic modeling shows that the reaction takes place under low temperatures (<470 °C) with a decrease from 3 to −4 in ΔFMQ.

$$(Mg,Fe)(Cr,Al,Fe)_2O_4\ (\text{ferrous chromite}) + 4(Mg,Fe)_2SiO_4\ (\text{olivine}) + 6H_2O\ (\text{fluids}) = Fe(Cr,Fe)_2O_4\ (\text{chromian magnetite}) + Fe_3O_4\ (\text{veined magnetite}) + 2Mg_3Si_2O_5(OH)_4\ (\text{antigorite}) + 2H_2 \quad (2)$$

Both temperature and oxygen fugacity of the major alteration stage can be constrained using pseudosection and chromite composition (Fig. 11, Fig. S3 and Fig. S4). Zn, Co, Mn and Ga are more sensitive to the alteration than the other elements, and their concentrations are rapidly changed from the magmatic chromite core to the ferrous chromite under temperatures of 603–556 °C and ΔFMQ of −0.3–2.4 (Fig. 10). Therefore, the magmatic chromites were strongly modified by the hydrothermal fluids as indicated by the microstructures and chemical compositions.

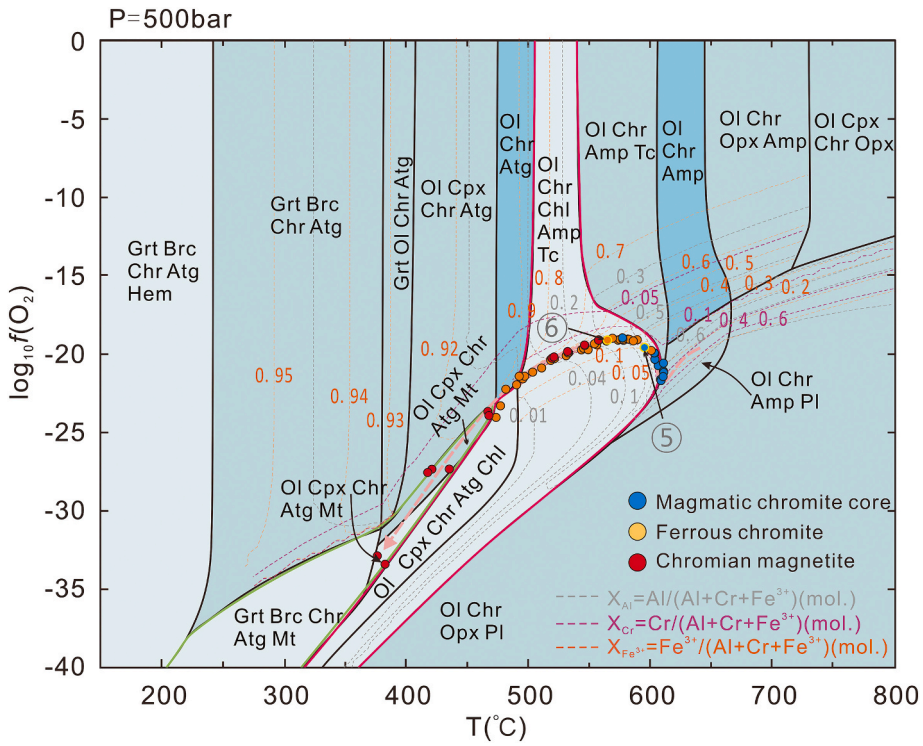

Fig. 10. T - $\log_{10}$ fO_2 pseudosection for the Jinchang serpentinite under pressures of 50 MPa. The filled circle marks compositional variations of the magmatic and altered chromite. Green bold line separates the fields containing Chr and Chr + Mt. The pink bold line surrounds the chlorite stability field. Grey, purple and orange dashed lines are contours of $X_{Al/Cr/Fe^{3+}}$ of chromite. The pink dashed line is the evolution path of chromite alteration. Points 5 and 6 with yellow outlines show the range of most drastic changes in trace element composition of chromite during alteration. Grt = garnet, Brc = brucite, Atg = antigorite, Chr = Chromite, Hem = hematite, Ol = olivine, Mt. = magnetite, Amp = amphibole, Cpx = clinopyroxene, Opx = orthopyroxene, Tc = talc, Chl = chlorite, Pl = plagioclase. (For interpretation of the references to colour in this figure legend, the reader is referred to the web version of this article.)

7. Tectonic implications of the Jinchang ophiolite

The Jinchang ophiolite experienced two stages of hydrothermal alteration, as well as slightly deformation. The first alteration took place at temperatures of 610–470 °C with ΔFMQ increasing from −1 to 3, consistent with high-temperature hydrothermal circulation of seawater in the lithospheric mantle. The second one occurred under low temperatures (<470 °C) with ΔFMQ decreasing from 3 to −4.

Electron backscattered diffraction (EBSD) was applied to reveal growth pattern of altered chromite. Chromian magnetite formation is interpreted as evidence for a coupled process of ferrous chromite dissolution and magnetite precipitation. The ferrous chromite, rich in Cr and Fe, has similar unit-cell parameters to those of the chromian magnetite, and thus can be used as a template for chromian magnetite growth (Fig. 3c and d). Breakdown of olivine, associated with dissolution of nanoscale magnetite grains which were initially formed in the host serpentinite, provide Fe required for chromian magnetite formation (Brunet, 2019). Two chromite grains are selected for determining mineral micro-structure. Grain A consists of the magmatic chromite core and altered chromian magnetite rim which have similar crystal orientation in close to ⟨100⟩ direction (Fig. 12c and g), and its profile (a-b) reveals both core and rims belong to a single crystal based on their low misorientation (<3°), indicating that chromian magnetite inherits the crystallographic orientation of the core (Fig. 12e). The grain B has variable misorientation ranging from 0 to 8° (Fig. 12f), indicating that its core and rim were deformed during the Late Triassic to Cenozoic obduction of the ophiolite after olivine serpentinization and chromite alteration.

The magmatic chromite in the Jinchang ophiolite have high Mg# and Cr# values, and low Al_2O_3 and TiO_2 contents, similar to those of chromite from the harzburgite of the Luobusa ophiolite (Fig. 5), the later shows refractory and depleted nature and are proposed to be SSZ-type ophiolite (Zhou et al., 2014). Despite the differences in trace element patterns between the Jinchang ophiolite and other tectonic settings, including komatiites, layered mafic-ultramafic intrusions, as well as the ophiolite from Thetford Mines in Cuba, and the Philippines (Fig. 6c; Pagé and Barnes, 2009; González-Jiménez et al., 2015; Song et al., 2020), there is a large overlap in trace element contents exists in different tectonic contexts. Therefore, the tectonic setting of host rock cannot be clearly identified from trace elemental composition of magmatic chromite by itself. Furthermore, the chromite was totally changed both in microstructures and elemental compositions during alteration, although the detailed processes are hard to be constrained. The use of trace element compositions as a proxy for tectonic settings may therefore be unreliable. The combination of different initial contents and the degree to which different processes have evolved may constitute a coincidence indicative of a wrong tectonic context.

8. Conclusions

(1) The magmatic chromite from the Jinchang ophiolite experienced subsolidus re-equilibration and hydrothermal alteration, and the two processes modified their microstructures and elemental compositions. The chromite minerals are depleted in Ni and enriched in Ga, V, Zn, Co, and Mn during the subsolidus re-equilibration, with a right-decline Zn-Co-Mn trend.

(2) The magmatic chromites further lose Ga and Sc, enrich Ni, Ti, Zn, Co and Mn elements during the hydrothermal alteration, and have a left-decline Zn-Co-Mn trend. The ferrous chromite is formed at the first stage of the hydrothermal alteration under high temperatures (610–470 °C) with an increase from −1 to 3 in ΔFMQ, whereas chromian magnetite is formed during the second one at low temperatures (<470 °C) with a decrease from 3 to −4

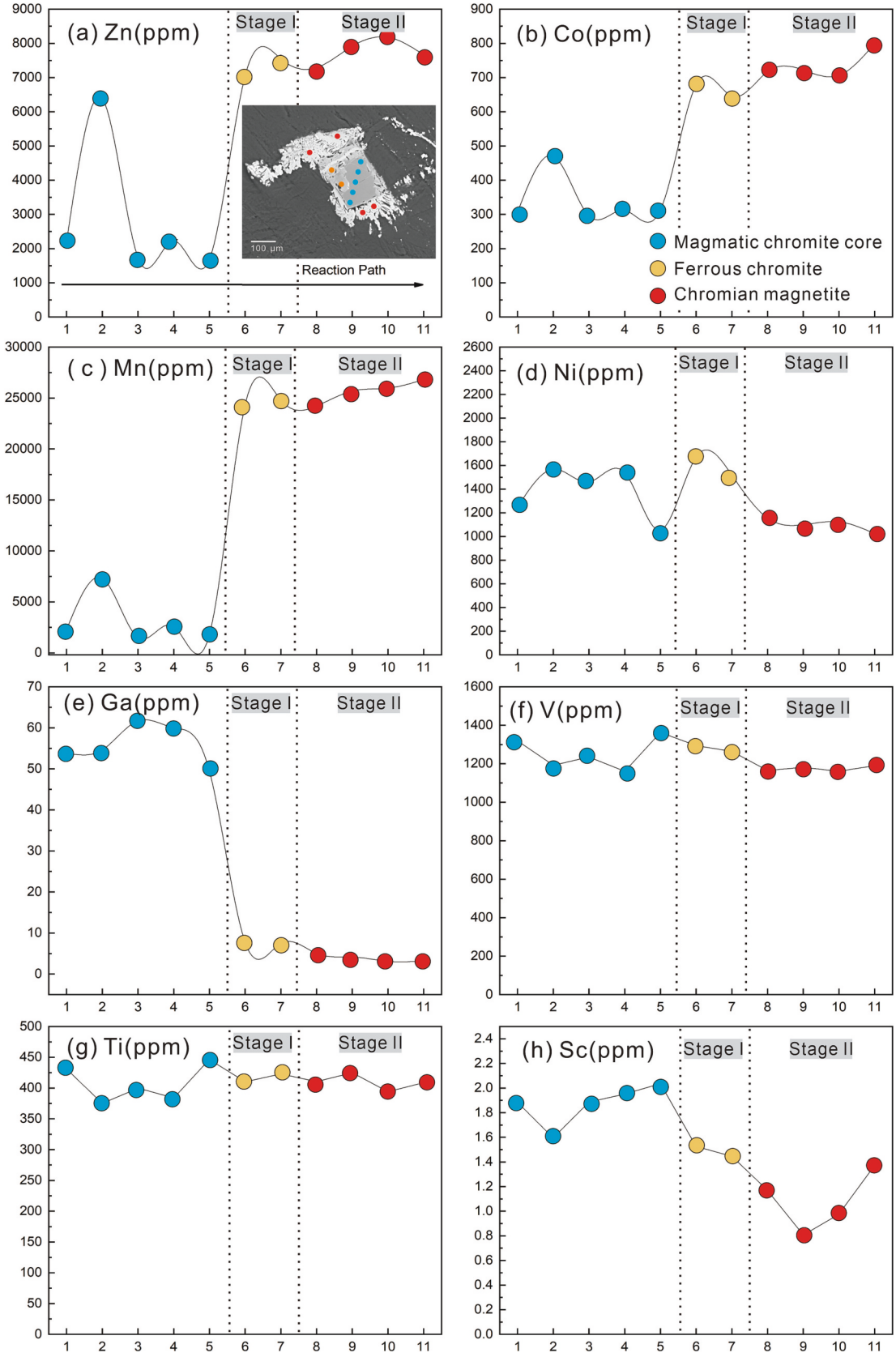

Fig. 11. Variation in the trace element composition of chromite. Three parts of altered chromite (magmatic chromite core, ferrous chromite and chromian magnetite) were analyzed within one particulate sample to remove the effects of magmatic processes and subsolidus exchange. The numbers on the horizontal coordinates of the diagram are sequential according to the order of the chromite composition shown in the Fig. 10 evolution pathway.

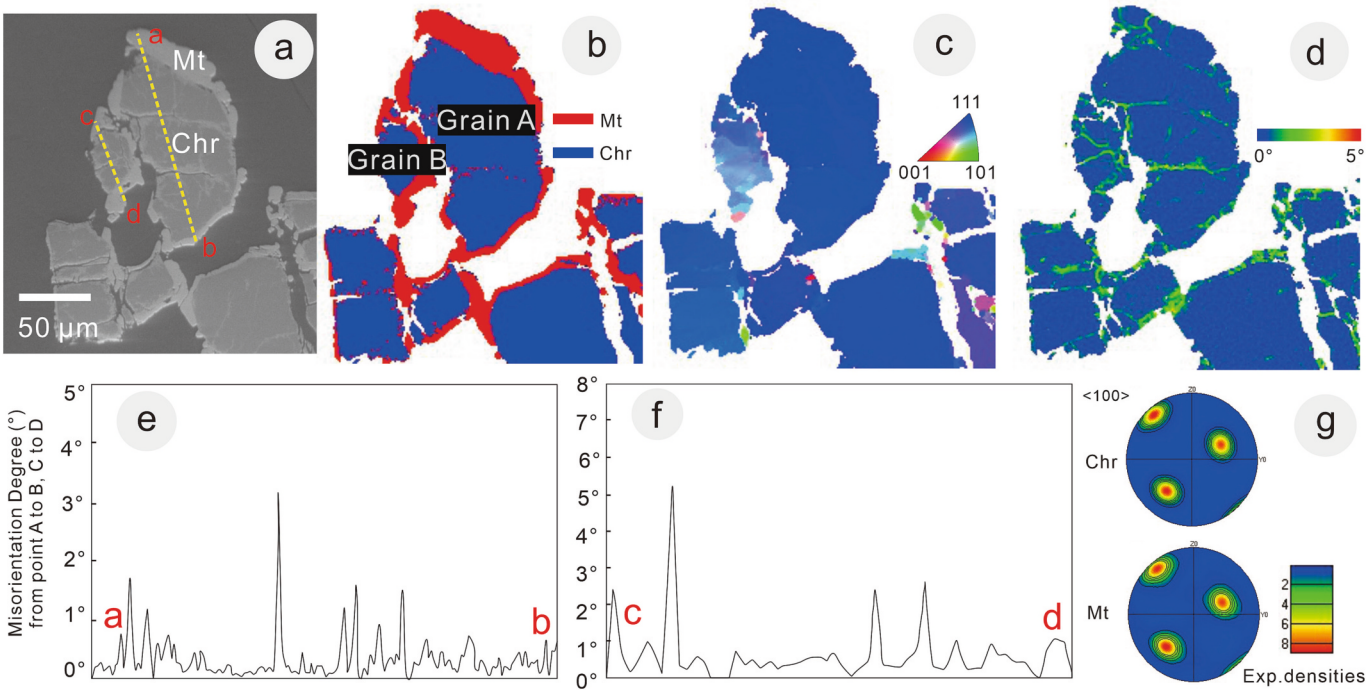

Fig. 12. EBSD analysis of the partially altered chromite. (a) SEM images for the magmatic chromite cores and chromian magnetite rims. (b) Phase distribution map illustrates the lithologic transition from magmatic chromite core to enclosing chromian magnetite rim. (c) IPF map shows all different orientations to identify crystal bending and subgrain boundaries. (d) Misorientation map of this chromite grain showing maximum misorientation below 5° relative to crystal orientation at the point A. (e) Misorientation profile along the dashed yellow line in (a) from point A to point B is shown relative to the point A; (f) Misorientation profile along the dashed yellow line in (a) is shown from the point C to D. (g) <100> pole figures show crystal orientation of magmatic chromite cores (top) and chromian magnetite rim (bottom) in (a). (For interpretation of the references to colour in this figure legend, the reader is referred to the web version of this article.)

in ΔFMQ. Trace elements were mainly changed during the first stage of alteration.

(3) Hydrothermal alteration may have taken place prior to the obduction of the Jinchang ophiolite during the Late Triassic to Cenozoic time. Considering that magmatic chromite minerals can be altered by the subsequent geological events; their elements should be paid much more attention when using them to address petrogenesis and discriminate tectonic environments.

Supplementary data to this article can be found online at https://doi.org/10.1016/j.lithos.2023.107385.

Declaration of Competing Interest

The authors declare that they have no known competing financial interests or personal relationships that could have appeared to influence the work reported in this paper.

Acknowledgments

This work was financially supported by the National Natural Science Foundation of China (42025203 and 41973031). Dr. Chang Xu is thanked for his help in EBSD analysis.

References

Arai, S., 1994. Characterization of spinel peridotites by olivine-spinel compositional relationships: Review and interpretation. Chem. Geol. 113, 191–204.
Balan, E., de Villiers, J.P.R., Eeckhout, S.G., Glatzel, P., Toplis, M.J., Fritsch, E., Allard, T., Galoisy, L., Calas, G., 2006. The oxidation state of vanadium in titanomagnetite from layered basic intrusions. Am. Mineral. 91, 953–956.
Banerjee, R., Mondal, S.K., Reisberg, L., Park, J.-W., 2022. Fractionation of trace and platinum-group elements during metamorphism of komatiitic chromites from the early Archean Gorumahishani greenstone belt, Singhbhum Craton (eastern India). Contrib. Mineral. Petrol. 177, 75.
Barnes, S.J., 2000. Chromite in Komatiites, II. Modification during Greenschist to Mid-Amphibolite Facies Metamorphism. J. Petrol. 41, 387–409.
Barnes, S.J., Roeder, P.L., 2001. The Range of Spinel Compositions in Terrestrial Mafic and Ultramafic Rocks. J. Petrol. 42, 2279–2302.
Bliss, N.W., Maclean, W.H., 1976. The paragenesis of zoned chromite from Central Manitoba. In: Irvine, T.N. (Ed.), Chromium: Its Physicochemical Behavior and Petrologic Significance. Pergamon, pp. 973–990.
Bordage, A., Balan, E., De Villiers, J.P.R., Cromarty, R., Juhin, A., Carvallo, C., Calas, G., Sunder Raju, P.V., Glatzel, P., 2011. V oxidation state in Fe–Ti oxides by high-energy resolution fluorescence-detected X-ray absorption spectroscopy. Phys. Chem. Miner. 38, 449–458.
Brunet, F., 2019. Hydrothermal production of H2 and Magnetite from Steel Slags: a Geo-inspired Approach based on Olivine Serpentinization. Front. Earth Sci. 7.
Burkhard, D.J., 1993. Accessory chromium spinels: their coexistence and alteration in serpentinites. Geochim. Cosmochim. Acta 57, 1297–1306.
Canales, J.P., Collins, J.A., Escartín, J., Detrick, R.S., 2000. Seismic structure across the rift valley of the Mid-Atlantic Ridge at 23°20′ (MARK area): Implications for crustal accretion processes at slow spreading ridges. J. Geophys. Res. Solid Earth 105, 28411–28425.
Colás, V., González-Jiménez, J.M., Griffin, W.L., Fanlo, I., Gervilla, F., O'Reilly, S.Y., Pearson, N.J., Kerestedjian, T., Proenza, J.A., 2014. Fingerprints of metamorphism in chromite: New insights from minor and trace elements. Chem. Geol. 389, 137–152.
Connolly, J.A.D., 2005. Computation of phase equilibria by linear programming: a tool for geodynamic modeling and its application to subduction zone decarbonation. Earth Planet. Sci. Lett. 236, 524–541.
Dare, S.A., Pearce, J.A., McDonald, I., Styles, M.T., 2009. Tectonic discrimination of peridotites using fO2–Cr# and Ga–Ti–FeIII systematics in chrome–spinel. Chem. Geol. 261, 199–216.
Dare, S.A.S., Barnes, S.-J., Beaudoin, G., Méric, J., Boutroy, E., Potvin-Doucet, C., 2014. Trace elements in magnetite as petrogenetic indicators. Mineral. Deposita 49, 785–796.
Eslami, A., Malvoisin, B., Brunet, F., Kananian, A., Bach, W., Grieco, G., Cavallo, A., Gatta, G.D., 2021. Podiform magnetite ore(s) in the Sabzevar ophiolite (NE Iran): oceanic hydrothermal alteration of a chromite deposit. Contrib. Mineral. Petrol. 176, 43.
Evans, B.W., Frost, B.R., 1975. Chrome-spinel in progressive metamorphism—a preliminary analysis. Geochim. Cosmochim. Acta 39, 959–972.
Evans, K.A., Powell, R., Frost, B.R., 2013. Using equilibrium thermodynamics in the study of metasomatic alteration, illustrated by an application to serpentinites. Lithos 168–169, 67–84.
Fang, N., 2003. Late Palaeozoic Ultramafic Lavas in Yunnan, SW China, and their Geodynamic significance. J. Petrol. 44, 141–158.

Gervilla, F., Padrón-Navarta, J.A., Kerestedjian, T., Sergeeva, I., González-Jiménez, J.M., Fanlo, I., 2012. Formation of ferrian chromite in podiform chromitites from the Golyamo Kamenyane serpentinite, Eastern Rhodopes, SE Bulgaria: a two-stage process. Contrib. Mineral. Petrol. 164, 643–657.

González-Jiménez, J.M., Locmelis, M., Belousova, E., Griffin, W.L., Gervilla, F., Kerestedjian, T.N., O'Reilly, S.Y., Pearson, N.J., Sergeeva, I., 2015. Genesis and tectonic implications of podiform chromitites in the metamorphosed ultramafic massif of Dobromirtsi (Bulgaria). Gondwana Res. 27, 555–574.

Grant, J.A., 1986. The isocon diagram; a simple solution to Gresens' equation for metasomatic alteration. Econ. Geol. 81, 1976–1982.

Guo, S., Ye, K., Chen, Y., Liu, J.-B., 2009. A Normalization solution to Mass transfer Illustration of Multiple Progressively Altered Samples using the Isocon Diagram. Econ. Geol. 104, 881–886.

Hasenclever, J., Theissen-Krah, S., Rüpke, L.H., Morgan, J.P., Iyer, K., Petersen, S., Devey, C.W., 2014. Hybrid shallow on-axis and deep off-axis hydrothermal circulation at fast-spreading ridges. Nature 508, 508–512. https://doi.org/10.1038/nature13174.

Holland, T., Powell, R., 1996. Thermodynamics of order-disorder in minerals; II, Symmetric formalism applied to solid solutions. Am. Mineral. 81, 1425–1437.

Holland, T.J.B., Powell, R., 2011. An improved and extended internally consistent thermodynamic dataset for phases of petrological interest, involving a new equation of state for solids: Thermodynamic Dataset for Phases of Petrological Interest. J. Metamorph. Geol. 29, 333–383.

Horn, I., Foley, S.F., Jackson, S.E., Jenner, G.A., 1994. Experimentally determined partitioning of high field strength- and selected transition elements between spinel and basaltic melt. Chem. Geol., Trace-Element Partition. Appl. Magmat. Process. 117, 193–218.

Hu, W., Zhong, H., Chu, Z., Zhu, W., Bai, Z., Zhang, C., 2020. Ancient Refertilization Process Preserved in the Plagioclase Peridotites: an example from the Shuanggou Ophiolite, Southwest China. J. Geophys. Res. Solid Earth 125.

Hu, W.-J., Zhou, M.-F., Yudovskaya, M.A., Vikentyev, I.V., Malpas, J., Zhang, P.-F., 2022. Trace elements in Chromite as Indicators of the Origin of the Giant Podiform Chromite Deposit at Kempirsai, Kazakhstan. Econom. Geol., Trace 117, 1629–1655.

Huang, J., Hao, J., Huang, F., Sverjensky, D.A., 2019. Mobility of chromium in high temperature crustal and upper mantle fluids. Geochem. Perspect. Lett. 12, 1–6.

Jennings, E.S., Holland, T.J.B., 2015. A simple Thermodynamic Model for Melting of Peridotite in the System NCFMASOCr. J. Petrol. 56, 869–892.

Jian, P., Liu, D., Kröner, A., Zhang, Q., Wang, Y., Sun, X., Zhang, W., 2009. Devonian to Permian plate tectonic cycle of the Paleo-Tethys Orogen in Southwest China (II): Insights from zircon ages of ophiolites, arc/back-arc assemblages and within-plate igneous rocks and generation of the Emeishan CFB province. Lithos 113, 767–784.

Kamenetsky, V.S., 2001. Factors Controlling Chemistry of Magmatic Spinel: an Empirical Study of Associated Olivine, Cr-spinel and Melt Inclusions from Primitive Rocks. J. Petrol. 42, 655–671.

Kimball, K.L., 1990. Effects of hydrothermal alteration on the compositions of chromian spinels. Contrib. Mineral. Petrol. 105, 337–346.

Klemme, S., Ivanic, T.J., Connolly, J.A.D., Harte, B., 2009. Thermodynamic modelling of Cr-bearing garnets with implications for diamond inclusions and peridotite xenoliths. In: Lithos, Proceedings of the 9th International Kimberlite Conference, 112, pp. 986–991.

Lai, C.-K., Meffre, S., Crawford, A.J., Zaw, K., Xue, C.-D., Halpin, J.A., 2014. The Western Ailaoshan Volcanic Belts and their SE Asia connection: a new tectonic model for the Eastern Indochina Block. Gondwana Res. 26, 52–74.

Li, P., Rui, G., Junwen, C., Ye, G., 2004. Paleomagnetic analysis of eastern Tibet: implications for the collisional and amalgamation history of the three Rivers Region, SW China. J. Asian Earth Sci. 24, 291–310.

Liu, Y., Hu, Z., Gao, S., Günther, D., Xu, J., Gao, C., Chen, H., 2008. In situ analysis of major and trace elements of anhydrous minerals by LA-ICP-MS without applying an internal standard. Chem. Geol. 257, 34–43.

McCollom, T.M., Bach, W., 2009. Thermodynamic constraints on hydrogen generation during serpentinization of ultramafic rocks. Geochim. Cosmochim. Acta 73, 856–875.

Mellini, M., Rumori, C., Viti, C., 2005. Hydrothermally reset magmatic spinels in retrograde serpentinites: formation of "ferritchromit" rims and chlorite aureoles. Contrib. Mineral. Petrol. 149, 266–275.

Metcalfe, I., 1996. Gondwanaland dispersion, Asian accretion and evolution of eastern Tethys*. Aust. J. Earth Sci. 43, 605–623.

Metcalfe, I., 2002. Permian tectonic framework and palaeogeography of SE Asia. J. Asian Earth Sci. 20, 551–566.

Metcalfe, I., 2013. Gondwana dispersion and Asian accretion: Tectonic and palaeogeographic evolution of eastern Tethys. J. Asian Earth Sci. 66, 1–33.

Mével, C., 2003. Serpentinization of abyssal peridotites at mid-ocean ridges. Compt. Rendus Geosci. 335, 825–852.

Mo, X.-X., Pan, G., 2006. From the Tethys to the formation of the Qinghai-Tibet Plateau: Constrained by tectono-magmatic events. Earth Sci. Front. 13, 43.

Mukherjee, R., Mondal, S.K., Rosing, M.T., Frei, R., 2010. Compositional variations in the Mesoarchean chromites of the Nuggihalli schist belt, Western Dharwar Craton (India): potential parental melts and implications for tectonic setting. Contrib. Mineral. Petrol. 160, 865–885.

Padrón-Navarta, J.A., Sánchez-Vizcaíno, V.L., Hermann, J., Connolly, J.A.D., Garrido, C. J., Gómez-Pugnaire, M.T., Marchesi, C., 2013. Tschermak's substitution in antigorite and consequences for phase relations and water liberation in high-grade serpentinites. Lithos 178, 186–196.

Pagé, P., Barnes, S.-J., 2009. Using Trace elements in Chromites to Constrain the Origin of Podiform Chromitites in the Thetford Mines Ophiolite, Quebec, Canada. Econ. Geol. 104, 997–1018.

Righter, K., Leeman, W.P., Hervig, R.L., 2006. Partitioning of Ni, Co and V between spinel-structured oxides and silicate melts: Importance of spinel composition. Chem. Geol. 227, 1–25.

Sack, R.O., Ghiorso, M.S., 1991. Chromian spinels as petrogenetic indicators: Thermodynamics and petrological applications. Am. Mineral. 76, 827–847.

Scowen, P.A.H., Roeder, P.L., Helz, R.T., 1991. Reequilibration of chromite within Kilauea Iki lava lake, Hawaii. Contrib. Mineral. Petrol. 107, 8–20.

Song, X.-Y., Wang, K.-Y., Barnes, S.J., Yi, J.-N., Chen, L.-M., Schoneveld, L.E., 2020. Petrogenetic insights from chromite in ultramafic cumulates of the Xiarihamu intrusion, northern Tibet Plateau, China. Am. Mineral. 105, 479–497.

Song, Z., Li, H., Li, L.-X., Ding, J.-H., Meng, J., 2021. Iron Isotopes and Trace Element Compositions of Magnetite from the Submarine Volcanic-Hosted Iron Deposits in East Tianshan, NW China: New Insights into the Mineralization Processes. J. Earth Sci. 32, 219–234.

Spandler, C., O'Neill, H.S.C., 2010. Diffusion and partition coefficients of minor and trace elements in San Carlos olivine at 1,300°C with some geochemical implications. Contrib. Mineral. Petrol. 159, 791–818.

Stampfli, G.M., Borel, G.D., 2002. A plate tectonic model for the Paleozoic and Mesozoic constrained by dynamic plate boundaries and restored synthetic oceanic isochrons. Earth Planet. Sci. Lett. 196, 17–33.

Su, B., 2022. Cretaceous Meteorite Impact-Induced initial Subduction: Records of highly Siderophile Element Abundances and Re-Os Isotopes in Ophiolites. J. Earth Sci. 33, 1526–1534.

Su, B., Zhou, M., Jing, J., Robinson, P.T., Chen, C., Xiao, Y., Liu, X., Shi, R., Lenaz, D., Hu, Y., 2019. Distinctive melt activity and chromite mineralization in Luobusa and Purang ophiolites, southern Tibet: constraints from trace element compositions of chromite and olivine. Sci. Bull. 64, 108–121.

Sverjensky, D.A., Harrison, B., Azzolini, D., 2014. Water in the deep Earth: the dielectric constant and the solubilities of quartz and corundum to 60kb and 1200°C. Geochim. Cosmochim. Acta 129, 125–145.

Toplis, M.J., Carroll, M.R., 1995. An Experimental Study of the Influence of Oxygen Fugacity on Fe-Ti Oxide Stability, Phase Relations, and Mineral–Melt Equilibria in Ferro-Basaltic Systems. J. Petrol. 36, 1137–1170.

Uysal, I., Akmaz, R.M., Saka, S., Kapsiotis, A., 2016. Coexistence of compositionally heterogeneous chromitites in the Antalya–Isparta ophiolitic suite, SW Turkey: A record of sequential magmatic processes in the sub-arc lithospheric mantle. Lithos 248–251, 160–174.

Wan, Z., Coogan, L.A., Canil, D., 2008. Experimental calibration of aluminum partitioning between olivine and spinel as a geothermometer. Am. Mineral. 93, 1142–1147.

Wang, X., Metcalfe, I., Jian, P., He, L., Wang, C., 2000. The Jinshajiang–Ailaoshan Suture Zone, China: tectonostratigraphy, age and evolution. J. Asian Earth Sci. 18, 675–690.

Wang, C.Y., Zhou, M.-F., Zhao, D., 2005. Mineral chemistry of chromite from the Permian Jinbaoshan Pt–Pd–sulphide-bearing ultramafic intrusion in SW China with petrogenetic implications. Lithos 83, 47–66.

Wood, B.J., Virgo, D., 1989. Upper mantle oxidation state: Ferric iron contents of lherzolite spinels by 57Fe Mössbauer spectroscopy and resultant oxygen fugacities. Geochim. Cosmochim. Acta 53, 1277–1291.

Wylie, A.G., Candela, P.A., Burke, T.M., 1987. Compositional zoning in unusual Zn-rich chromite from the Sykesville District of Maryland and its bearing on the origin of" ferritchromit". Am. Mineral. 72, 413–422.

Yang, L., Wang, Q., Wang, Y., Li, G., 2018. Proto- to Paleo-Tethyan evolution of the eastern margin of Simao block. Gondwana Res. 62, 61–74.

Yumul, G.P., Zhou, M.-F., Wang, C.Y., Zhao, T.-P., Dimalanta, C.B., 2008. Geology and geochemistry of the Shuanggou ophiolite (Ailao Shan ophiolitic belt), Yunnan Province, SW China: evidence for a slow-spreading oceanic basin origin. J. Asian Earth Sci. 32, 385–395.

Zhang, Q., Zhou, D., Li, X., Chen, Y., 1995. Characteristics and genesises of Shuanggou ophiolites, Yunnan Province. China Acta Petrol. Sin. (in Chinese) 11, 190–202.

Zhao, J.-H., Zhou, M.-F., Yan, D.-P., Zheng, J.-P., Li, J.-W., 2011. Reappraisal of the ages of Neoproterozoic strata in South China: no connection with the Grenvillian orogeny. Geology 39, 299–302.

Zhao, J.-H., Asimow, P.D., Zhou, M.-F., Zhang, J., Yan, D.-P., Zheng, J.-P., 2017. An Andean-type arc system in Rodinia constrained by the Neoproterozoic Shimian ophiolite in South China. Precambrian Res. 296, 93–111.

Zhou, M.-F., Robinson, P.T., Su, B.-X., Gao, J.-F., Li, J.-W., Yang, J.-S., Malpas, J., 2014. Compositions of chromite, associated minerals, and parental magmas of podiform chromite deposits: the role of slab contamination of asthenospheric melts in suprasubduction zone environments. Gondwana Res. 26, 262–283.